



Physical and Welding Metallurgy of Gd-Enriched Austenitic Alloys for Spent Nuclear Fuel Applications — Part I: Stainless Steel Alloys

The solidification temperature range of these alloys was found to be very large, leading to poor hot ductility and weldability

BY J. N. DUPONT, C. V. ROBINO, J. R. MICHAEL, R. E. MIZIA, AND D. B. WILLIAMS

ABSTRACT. The development of Gd-enriched austenitic alloys is currently being considered for nuclear criticality control in spent nuclear fuel storage applications. In this research, the physical and welding metallurgy of Gd-enriched austenitic alloys has been investigated with a combination of differential thermal analysis, Vareststraint and Gleeble tests, and various microstructural characterization techniques. The results of Gd additions made to a 316L stainless steel-type matrix are presented in this article, and similar information is provided for Gd-enriched Ni-based alloys in the Part II companion article.

Type 316L stainless steel alloys with up to 6 wt-% Gd were observed to solidify in the primary ferrite mode and terminate solidification by a peritectic reaction involving a $(\text{Fe,Ni,Cr})_3\text{Gd}$ intermetallic that is rich in Ni and Gd. The ferrite partially transforms to austenite after solidification by a solid-state transformation, producing a final microstructure that has an austenitic matrix with remnant ferrite at the dendrite cores and interdendritic $(\text{Fe,Ni,Cr})_3\text{Gd}$. Essentially no Gd is dissolved in either the ferrite or austenite phases. Heating of the as-cast alloys leads

to liquation of the $(\text{Fe,Ni,Cr})_3\text{Gd}$ intermetallic at $\sim 1060^\circ\text{C}$, and this phase reforms at a similar temperature during solidification. As a result, the solidification temperature range of these alloys is very large ($360^\circ\text{--}400^\circ\text{C}$, depending on Gd concentration). The large solidification temperature range leads to poor hot ductility and weldability, and limits production of these materials on a commercial basis. In Part II of this article, it is demonstrated that the solidification response and resultant hot ductility and weldability are significantly improved with the use of Ni-based matrix compositions.

Introduction

Safe disposition of spent nuclear fuel owned by the United States Department of Energy requires the development of thermal neutron-absorbing structural materials for nuclear criticality control. As shown schematically in Fig. 1, these materials will be used for the internal baskets that separate spent fuel assemblies and are required for structural support, spent nuclear fuel geometry control, and nuclear criticality safety. Given the large quantity of material required for this ap-

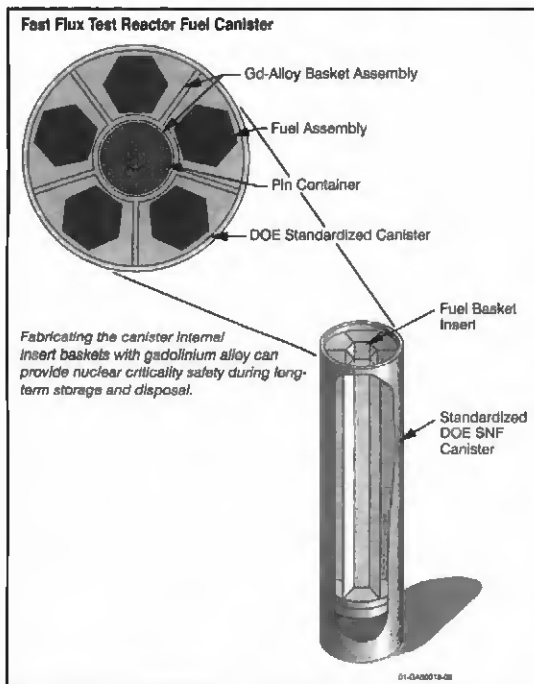
plication, the material should be producible with conventional fabrication methods such as ingot casting and hot working. Ultimately, the material will be formed and welded into an internal structure that will cradle the fuel and maintain a specified geometry (Ref. 1), so the material must also exhibit good weldability. In addition, the basket materials must be corrosion resistant under the projected storage conditions.

Previous research on selection of candidate alloys that could meet these requirements considered stainless steels containing boron (Refs. 2, 3). While these alloys are available as ASME code-approved materials, gadolinium (Gd) is significantly more effective than boron as an alloy addition for neutron absorption for two reasons. First, Gd has a significantly higher neutron absorption cross section than boron (765 barn for boron compared to 48,800 barn for Gd) (Ref. 4). Thus, Gd additions could potentially provide a means for handling the highly enriched fuel that cannot currently be handled with boron-containing stainless steel alloys. The higher thermal neutron absorption capacity may also allow thinner sections of this material to be used, which may be important to ensure the total weight of the canister stays within prescribed limits. Second, Gd-containing constituents in the alloy may not dissolve as quickly as chromium borides in the presence of water during basket material degradation due to long-term corrosion (Ref. 4). Therefore, there is interest in the use of Gd-containing alloys for storage, transportation, and disposal of spent nuclear fuel. However, unlike stainless steel alloys containing boron, there has been

J. N. DUPONT is Associate Professor and D. B. WILLIAMS is Vice Provost for Research and a Professor, Department of Materials Science & Engineering, Lehigh University, Bethlehem, Pa. C. V. ROBINO is with the Technical Staff, Joining and Coating Department, and J. R. MICHAEL is with the Technical Staff, Materials Characterization Dept., Sandia National Laboratories, Albuquerque, N.Mex. R. E. MIZIA is Engineering Fellow, Energy and Engineering Technology, Idaho National Engineering and Environmental Laboratory, Idaho Falls, Idaho.

KEYWORDS

Gadolinium-Enriched
Stainless Steel
Austenitic Alloys
Solid-State Transformation
Weldability
Ductility
Solidification Cracking



very little research on production and welding of Gd-containing austenitic alloys.

There have been very few studies of Gd-alloyed materials produced by conventional ingot metallurgy practice (Refs. 5–8). In addition, there are very little data available concerning the physical metallurgy of Gd-enriched alloys that can be used as a guide to develop weldable alloys that can be produced by conventional methods. Phase equilibria data are virtually nonexistent, and the only available information concerning the relevant ternary systems consists of a partial isothermal section (at 25°C) for the Fe-Ni-Gd system (Ref. 5). Phase diagrams for the relevant binary systems, e.g., Fe-Gd, Ni-Gd, and Cr-Gd, are available (Ref. 6), and these indicate that the Fe-Gd and Ni-Gd systems both contain numerous intermetallic phases and complex solidification reaction sequences. In particular, peritectic

reaction sequences appear to dominate the formation of intermetallic compounds in these systems (with the notable exception for low Gd levels in the Ni-Gd system, where a eutectic reaction is observed). A detailed study of phase equilibria and solidification paths in the related Fe-Mo-Gd system (Ref. 7) revealed extremely complex solidification behavior in these alloys. In this system, nine binary invariant solidification reactions and eight ternary invariant reactions were observed. It is known that a very limited quantity of Gd-alloyed austenitic stainless steel was produced in the 1960s by a major stainless steel supplier (Ref. 8). However, the results of that work are considered proprietary by the producer, so that little is known of the composition ranges examined, processing response, microstructures, or resultant weldability.

The objective of this research is to investigate the development of weldable, Gd-enriched austenitic alloys for spent nuclear fuel storage applications. The results of Gd additions made to a stainless steel matrix are provided in this first article. These results revealed significant technical chal-

Fig. 1 — Illustration of standardized canister assembly for transportation and long-term storage of spent nuclear fuel owned by the Department of Energy.

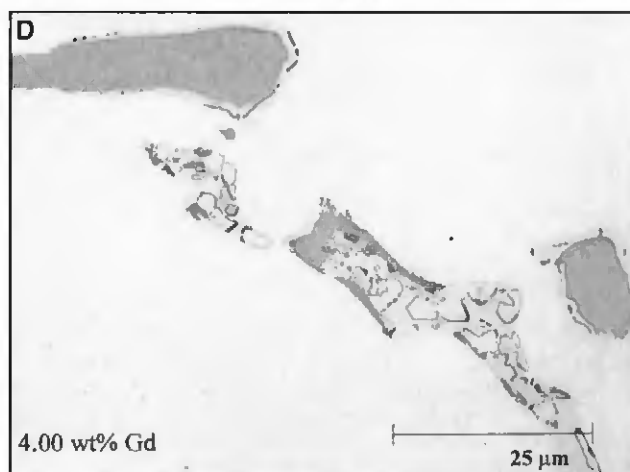
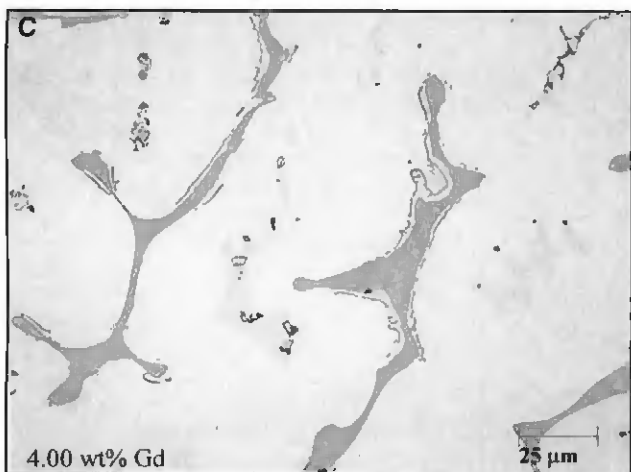
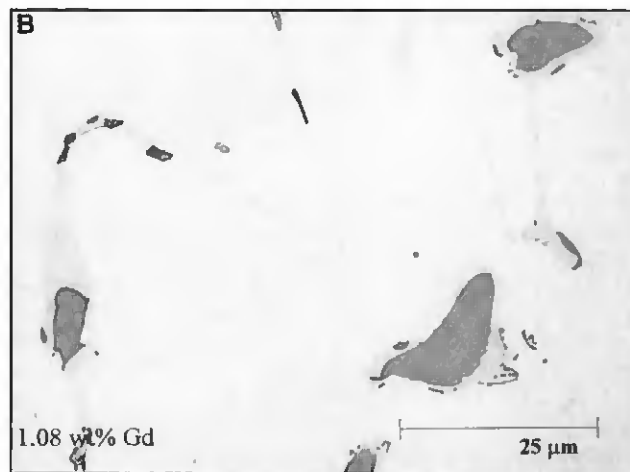
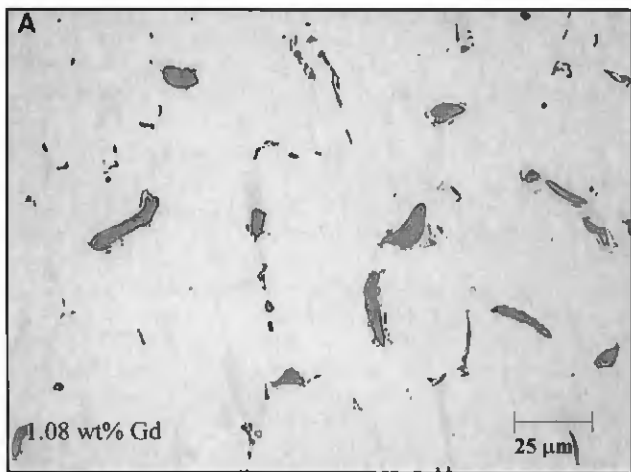


Fig. 2 — LOM photomicrographs. A, B — 1.08 wt-% Gd alloy; C, D — 4.00 wt-% Gd alloy.

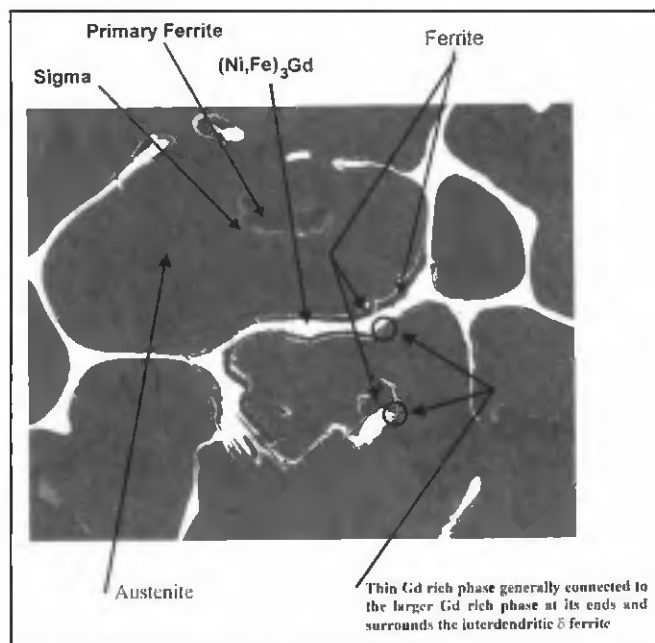


Fig. 3 — Backscattered SEM photomicrograph of 4.0 wt-% Gd alloy.

allenges to the development of weldable Gd-enriched stainless steel alloys produced with conventional hot working techniques. Subsequent research has shown that these obstacles can be surmounted with Gd additions made to a nickel alloy matrix, and the results of that research are summarized in the Part II companion article (Ref. 9).

Experimental Procedure

Eight stainless steel alloys with various Gd concentrations were melted by vacuum induction heating. The ingots were ~100 mm square by 75 cm long. Details on the melting procedure can be found in Ref. 10. The compositions of these heats are provided in Table 1. A Gd-free 316L stainless steel was prepared as a baseline for comparison and is labeled 316L in Table 1. The remaining Gd-enriched alloys are identified according to their target nominal Gd concentrations (0.4, 1, 2, 4, and 6 wt-% Gd). The nominal compositions were selected to provide a Type 316L matrix composition that would be expected to solidify in a primary ferrite mode. Results of recent research (Ref. 11) has shown that these alloys form a Ni-rich (Fe,Ni,Cr)₃Gd intermetallic phase that depletes the matrix of Ni and enriches the matrix in Cr, Mo, and Mn. Thus, in order to produce a matrix composition similar to that of 316L, adjustments to the nominal Ni, Cr, Mo, and Mn concentrations are required to compensate for these alloy enrichment and depletion effects. (This is described in more detail in the Discussion section.) Two heats were produced of alloys 0.4 and 1 wt-% Gd. The heats marked

"A" were used in the as-cast condition for differential thermal analysis and hot ductility testing. These test results were needed to select optimum hot working temperatures for the as-cast ingots. Alloys 0.4-B, 1-B, and 2 were reduced into plate by hot forging. (Alloys 4 and 6 were used for testing only in the as-cast form.) Initial forging attempts and subsequent hot ductility results indicated that the alloys were sensitive to hot tearing at temperatures above approximately 1060°C and that the maximum ductility was achieved at approximately 950°C. Thus, the hot forging was conducted in two separate steps. In the first step, the ingots were heated to 950°C and hot forged to a thickness of approximately 50 mm. Individual reductions of 12 mm were used. Each ingot received one or two reductions at a time before it was returned to the furnace for reheating. After reduction to approximately 50 mm, the ingots were allowed to cool and then sectioned into smaller lengths for easier handling in the hot forge. The smaller lengths were then reheated to 950°C and given a final reduction to plate that was approximately 19 mm thick and 115 mm wide. The final reduction was accomplished in two to three sets of smaller reductions. After reduction, the ingots were annealed at 980°C for one hour and water quenched.

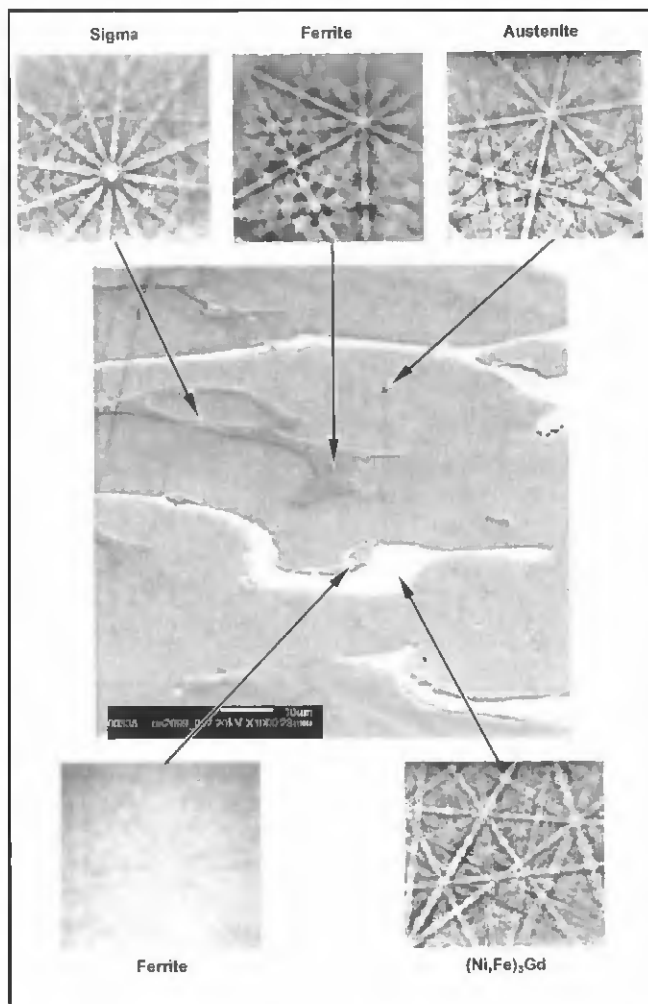


Fig. 4 — Typical BEKP patterns acquired from various phases in the 4 wt-% Gd alloy.

Gleeble hot ductility tests were conducted on cylindrical bars 102 mm long and 6.35 mm in diameter with threaded ends. The samples were heated in the Gleeble to the test temperature of interest at a rate of 100°C/min and held for 1 min at temperature. During this 1 min, the temperature was adjusted to the desired test temperature. The sample was then pulled in tension at a cross-head speed of 1 mm/s. Type K thermocouples were used to monitor the temperature. Testing was done in a vacuum of ~100 millitorr to reduce oxidation and prevent detachment of the thermocouples. The reduction in area of the failed samples was determined as a measure of the hot ductility.

Reaction temperatures during melting and solidification were measured using differential thermal analysis (DTA). The DTA was conducted on a Netzsch STA 409 differential thermal analyzer using 500- to 550-mg samples. The DTA system was calibrated to within 2°C using a pure Ni standard (melting point = 1455°C). Samples were melted and solidified under flowing

Table 1 — Experimental Heat Compositions (values in wt-%)

Alloy	Fe	Ni	Cr	Mo	Mn	Si	Gd	P	S	N	C
316L	Bal.	11.52	16.64	2.76	1.73	0.12	—	<0.001	0.002	0.009	0.005
0.4-A	Bal.	11.66	16.52	2.70	1.70	0.14	0.45	<0.001	<0.001	0.009	0.008
0.4-B	Bal.	11.45	16.47	2.75	1.62	0.11	0.38	0.002	0.002	0.003	<0.01
1-A	Bal.	11.94	16.30	2.63	1.69	0.10	1.08	<0.001	<0.001	0.008	0.012
1-B	Bal.	11.81	16.37	2.74	1.91	0.13	0.89	0.003	0.002	0.004	<0.01
2	Bal.	12.22	16.12	2.74	1.60	0.09	1.89	<0.001	<0.001	0.001	0.008
4	Bal.	13.06	15.30	2.50	1.55	0.17	4.00	<0.001	<0.001	0.001	0.006
6	Bal.	13.86	14.69	2.38	1.48	0.18	5.84	<0.001	<0.001	0.001	0.005

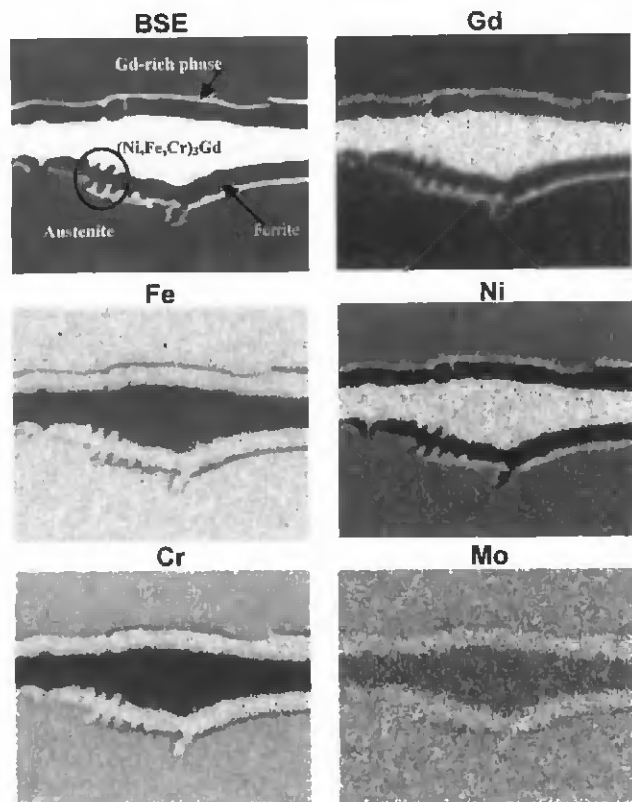


Fig. 5 — EDS spectrum images that qualitatively illustrate the distribution of alloying elements in the austenite, ferrite, and Gd-rich phases present in the interdendritic region.

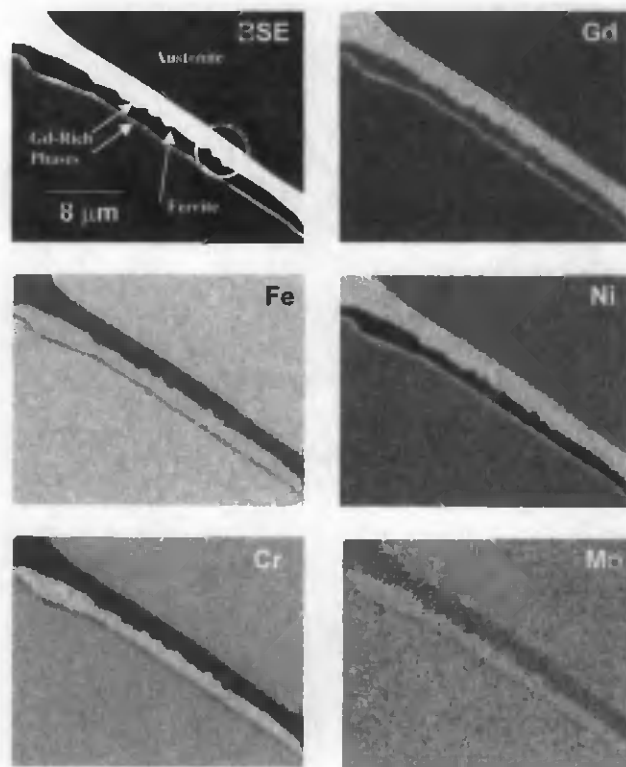


Fig. 6 — EDS spectrum images that illustrate the distribution of alloying elements in the austenite, ferrite, and Gd-rich phases present in the interdendritic region.

argon in alumina crucibles, and pure alumina was used as the reference material. The samples were packed in alumina powder to prevent oxidation. Preliminary tests were conducted to establish the liquidus temperature of each alloy. After these preliminary tests, the samples were heated at a rate of 5°C/min to approximately 10°C above their liquidus. The samples were then cooled at 5°C/min to determine the temperatures of reactions that occur during solidification. Reaction temperatures were taken as deviations from the local baseline. Weldability tests were conducted with the Varestraint test. The Varestraint tests were conducted on alloys 0.4-B, 1-B, and 2. The samples were removed from the annealed plate and machined to 165

mm long × 25 mm wide × 6.4 mm thick. The welding parameters were 100 A, 9 V, and 3 mm/s travel speed. A constant augmented strain level of 3.5% was used.

Light optical microscopy (LOM) was conducted on samples polished through 0.04-μm colloidal silica. Scanning electron microscopy (SEM) was performed using a JEOL 6300 field emission gun scanning electron microscope (FEG-SEM) at an accelerating voltage of 15 kV. Electron probe microanalysis (EPMA-WDS) was conducted on a JEOL 733 probe at an accelerating voltage of 15 kV and beam current of 20 nA. All EPMA samples were mounted in thermal setting epoxy, polished flat to a 0.03-μm finish using an alumina slurry, ultrasonically cleaned in

acetone, and carbon coated prior to analysis. Pure element standards were used for calibration, and raw data were reduced to weight percentages using a ZAF algorithm (Ref. 12).

Backscattered electron Kikuchi patterns, also known as electron backscattering patterns (EBSP), were collected using a JEOL 6400 SEM and a charge-coupled device (CCD) based camera system. Patterns were obtained from samples using a 20-kV accelerating voltage, 10-nA beam current, and 70-deg specimen tilt. The patterns were collected by stopping the electron beam on the feature or area of interest. The CCD camera acquisition time is controlled by automatic blanking of the SEM electron beam. Typical exposure

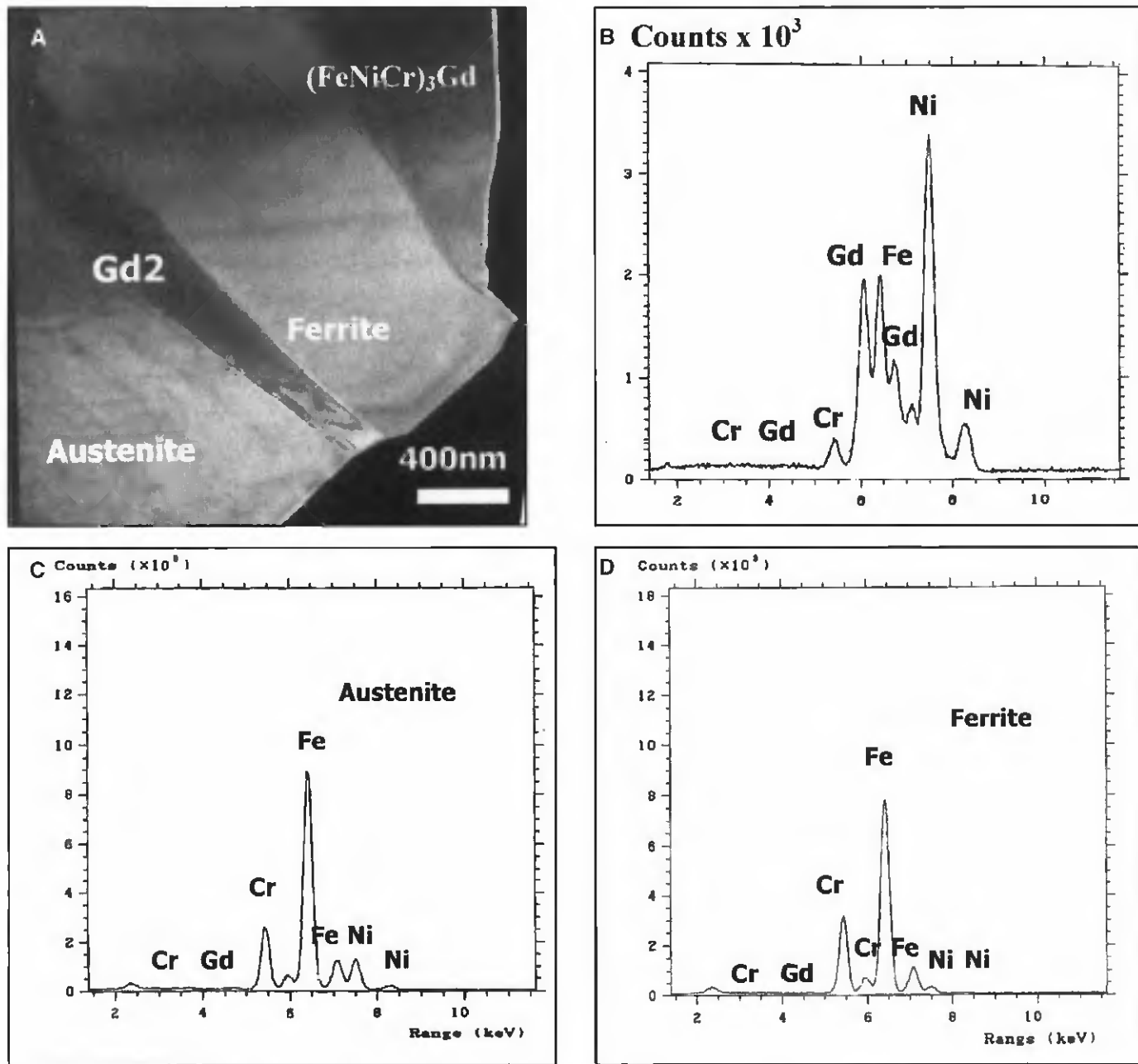


Fig. 7 — A — Dark-field TEM photomicrograph; and EDS spectra acquired from the following: B — Gd-rich phases; C — austenite; and D — ferrite in 6 wt-% Gd alloy.

times for this study were in the range of 2 to 10 s. The raw patterns were corrected for the background intensity using a flat-folding procedure. Qualitative chemistry information was obtained through energy dispersive X-ray spectrometry (EDS), and the crystallographic information was automatically extracted from the patterns using software developed at Sandia National Laboratories. The crystallographic information along with the qualitative chemistry information were used to search the International Center for Diffraction Data (ICDD) Powder Diffraction File (PDF).

Specimens for transmission electron

microscopy (TEM) were prepared by initially cutting samples into 2-mm-thick slices. The slices were ground from both sides to a thickness of approximately 150 μm using a series of 300, 600, 800, and 1200 SiC sandpapers. Slices were then cut into a 3-mm-diameter disc using a Gatan punch. The discs were polished to approximately 80 μm and thinned again to approximately 30 μm by dimpling. Final preparation of the foils was accomplished by ion beam thinning in a precision ion polishing system. Thin foils were examined using a JEOL 2000FX transmission electron microscope (TEM) equipped with an Oxford 2000 II energy-dispersive

spectrometer (EDS) for qualitative chemical analysis. The accelerating voltage was 200 kV, and a double tilt specimen holder was used so that the specific orientation could be obtained. Imaging was conducted in both dark and bright field modes. Crystal structure information was obtained with the selected area diffraction (SAD) technique.

Results

As-Cast Microstructures

As previously mentioned, no information exists in the open literature on phase

Table 2 — Distribution of Alloying Elements in Austenite, Interdendritic Ferrite, and (Fe,Ni,Cr)₃Gd Phases Observed in Alloy 6 (All values listed in wt-%.)

Phase	Fe	Ni	Cr	Mo	Si	Gd
Austenite	66.6 ± 0.3	11.4 ± 0.2	15.7 ± 0.2	2.6 ± 0.1	< 0.1	< 0.1
Ferrite	66.7 ± 2.4	2.3 ± 0.3	23.5 ± 2.0	4.2 ± 0.2	< 0.1	< 0.2
(Fe,Ni,Cr) ₃ Gd	19.6 ± 1.7	27.8 ± 2.4	1.7 ± 0.2	< 0.1	1.5 ± 0.5	49.0 ± 0.9

Table 3 — WRC Ni_{eq} and Cr_{eq} Values and Expected Solidification Mode for Each Alloy

Alloy	Ni _{eq}	Cr _{eq}	Solidification Mode
0.4-A	12.1	19.2	FA
0.4-B	11.9	19.2	FA
1-A	12.5	18.9	FA
1-B	12.2	19.1	FA
2	12.5	18.9	FA
4	13.3	17.8	AF
6	14.1	17.1	ΔF

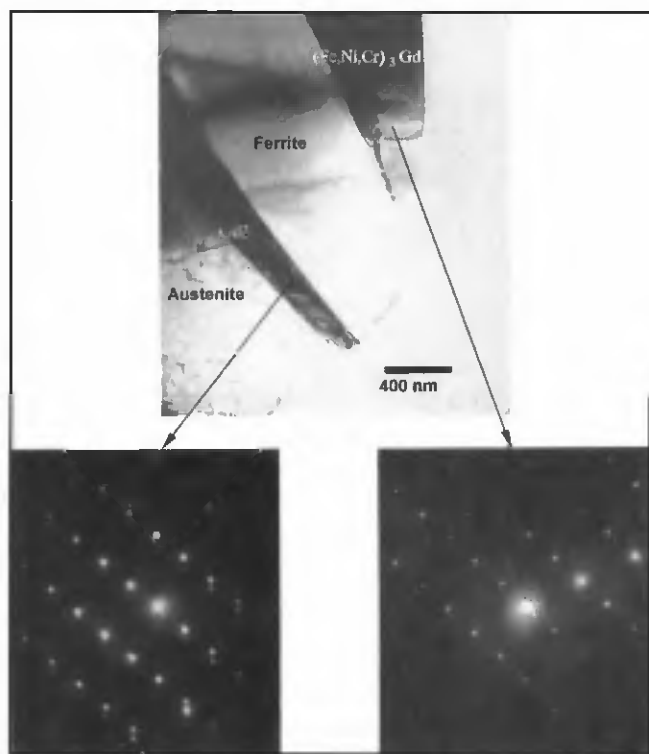


Fig. 8 — Bright field image and selected area diffraction patterns from major and thin gadolinium-containing constituents.

equilibria of Gd-enriched stainless steels. Thus, this section summarizes the types of phases that form during solidification of the ingots, which, as shown later, have a strong influence on the hot ductility and weldability of these alloys. Figure 2 shows typical low and high magnification LOM photomicrographs of alloys 1-A and 4 in the as-cast condition. Apart from the relative phase fractions, the microstructural features observed in these two alloys were typical of the remaining experimental alloys. Figure 3 shows a backscattered electron photomicrograph of alloy 4 in which the various phases are labeled, and Fig. 4 shows typical backscattered diffraction patterns acquired from each phase that were utilized for the phase identification. The as-cast microstructures contain four phases: the austenite matrix, delta ferrite, sigma, and an intermetallic (Fe,Ni,Cr)₃Gd phase. The (Fe,Ni,Cr)₃Gd phase appears

throughout the microstructure — in the cell cores and in the interdendritic regions. Often, there is a very thin Gd-rich phase adjacent to the major (Fe,Ni,Cr)₃Gd phase in the interdendritic area, which was too small to identify with EBSD. This Gd-containing region is generally connected to the major gadolinide at its ends (in the two-dimensional polished section), and surrounds the interdendritic delta ferrite (see circled regions in Fig. 3).

Figures 5 and 6 show a backscattered SEM image (labeled BSE) and EDS spectrum images that qualitatively illustrate the distribution of alloying elements in the austenite, ferrite, and Gd-rich phases present in the interdendritic region. EDS maps for Fe, Ni, Cr, Mo, and Gd are shown. The delta ferrite is enriched in Cr and Mo and depleted in Ni relative to the austenite matrix. This segregation behav-

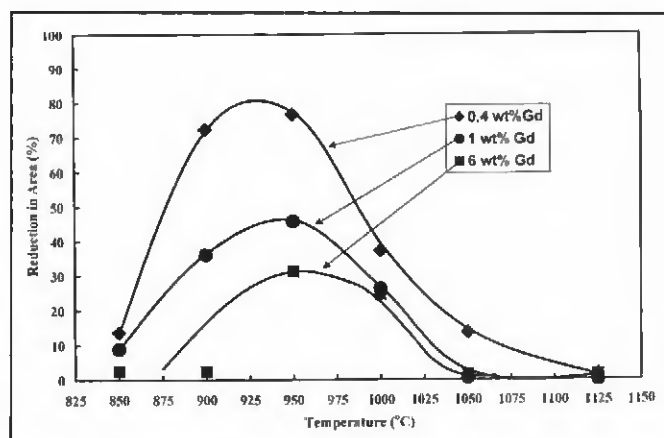


Fig. 9 — Reduction in area as a function of temperature for 0.4, 1.0, and 6.0 wt-% Gd alloys.

ior is typically observed between ferrite and austenite in stainless steels (Ref. 12). Cr and Mo each have identical crystal structures as delta ferrite (body-centered cubic) and thus exhibit higher solubility in the delta ferrite. Similarly, Ni and the austenite matrix are each face-centered cubic, and Ni preferentially segregates to the austenite. There is a subtle difference between Figs. 5 and 6 that is important to note. In Fig. 5, the thin Gd-rich phase is present on each side of the larger (Fe,Ni,Cr)₃Gd phase. When this morphology was observed, ferrite was also present on each side of the larger (Fe,Ni,Cr)₃Gd phase. However, as shown in Fig. 6, when the thin Gd-rich phase was not present on one side of the larger (Fe,Ni,Cr)₃Gd phase, the ferrite was not observed on that side either. In addition, as the circled areas on the BSE images of Figs. 5 and 6 show, the thin Gd-rich constituent and the major gadolinide often have oscillating features along their interfaces with the intervening ferrite. In cases where the oscillating features are present on both the thin and major constituents (as in Fig. 5), it often appears that the oscillations are coupled. The significance of these observations are discussed later when the transformation sequence of these alloys is described.

Electron probe microanalysis was con-

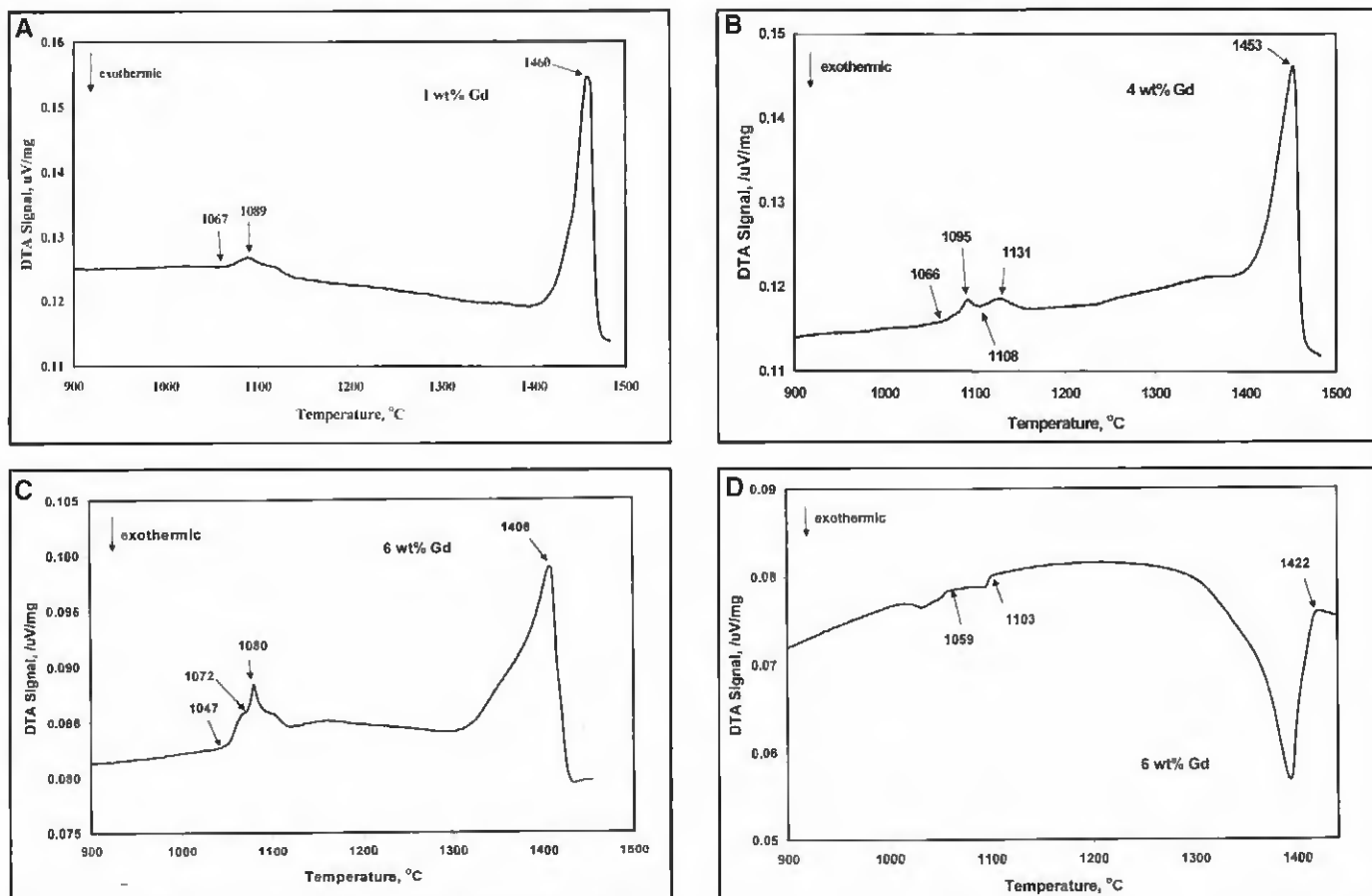


Fig. 10 — DTA scans acquired on alloys with the following conditions: A — 1 wt-% Gd, heating; B — 4 wt-% Gd, heating; C — 6 wt-% Gd, heating; and D — 6 wt-%, cooling.

ducted on alloy 6 to determine the composition of each phase, and the results are listed in Table 2. Note that the target austenite matrix composition is very close to that required for 316L (10–14 wt-% Ni, 16–18 wt-% Cr). The slightly low Cr in the austenite results from the high Cr content observed in the interdendritic ferrite (23.5 wt-% Cr). The composition of the $(\text{Fe,Ni,Cr})_3\text{Gd}$ is consistent with the stoichiometry of this phase. There is essentially no solubility of Gd in the austenite matrix or ferritic constituents. This indicates that essentially all the Gd is contained in the Gd-rich intermetallic constituents.

As described above, the $(\text{Fe,Ni,Cr})_3\text{Gd}$ phase in the interdendritic regions is relatively coarse and often accompanied by a very thin ($< 0.1 \mu\text{m}$) Gd-rich phase. Positive identification of this thin Gd-rich phase was not possible by EPMA or EBSD because its size is beyond the resolution limit of these techniques. Thus, a TEM investigation of thin foils was performed. For this study, a region of alloy 6 was selected that contained both the coarse $(\text{Fe,Ni,Cr})_3\text{Gd}$ intermetallic and the smaller Gd-rich phase. Figure 7 shows a dark field TEM image in which each Gd

phase is identified. The major $(\text{Fe,Ni,Cr})_3\text{Gd}$ constituent was identified previously by EBSD and the smaller Gd phase is labeled Gd2 in Fig. 7. Energy-dispersive spectrometry spectra were obtained from both phases and were identical within the expected errors of counting statistics, which is $\pm 10\%$ relative (only one spectra is shown in Fig. 7). The EDS spectra from the intervening ferrite is reduced in Ni compared to the EDS spectrum from the austenite. The austenite is relatively low in Cr and enriched in Fe. These data compare well with the EDS spectrum images displayed in Figs. 5 and 6. The TEM-EDS spectra provide a preliminary indication that the two Gd phases are identical. However, diffraction evidence is required for positive identification since it is possible for two phases to have similar compositions, but different crystal structures.

Figure 8 shows a bright field image and SAD patterns from the $(\text{Fe,Ni,Cr})_3\text{Gd}$ and Gd2 constituents. The similarity of the two SAD patterns indicate that the two constituents are the same phase in essentially the same orientation, and measurement of the average diffraction spot spacing and pattern angles confirms this similarity.

Note that there are a few spots in the SAD patterns (particularly from the $(\text{Fe,Ni,Cr})_3\text{Gd}$ phase) that seem not to be in the same array as most of the other spots. The SAD patterns were obtained from regions at best $\sim 0.5 \mu\text{m}$ in diameter, in which case the diffraction spots from the surrounding ferrite and/or austenite may also contribute to the pattern. Convergent beam electron diffraction analysis of the gadolinide constituents yielded results that confirmed the SAD observations. Thus, the TEM data confirm that both Gd-containing constituents have identical structure and orientation and, when combined with the EDS and EBSD data, prove that both are $(\text{Fe,Ni,Cr})_3\text{Gd}$.

Hot Ductility and Solidification Behavior

The hot ductility behavior of engineering alloys is important from both hot working and weldability perspectives. In general, alloys that possess good ductility at temperatures approaching the melting temperature can typically be hot worked easily and welded without cracking problems in the heat-affected zone. Conversely, loss of ductility at temperatures well below melting usually signals poten-

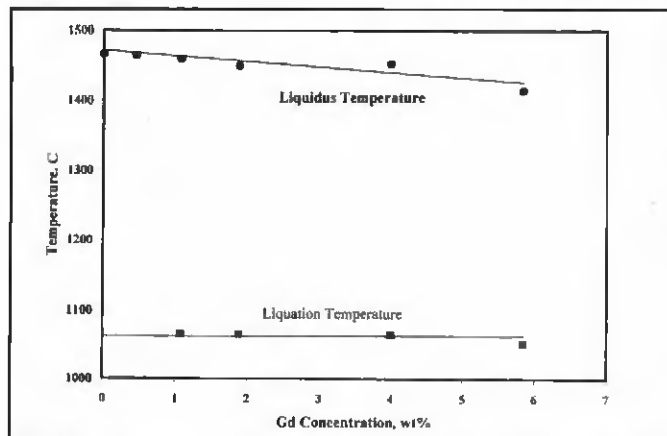


Fig. 11 — Variation in liquidus and liquation temperatures with gadolinium concentration.

tial problems with hot working and heat-affected zone cracking. Similarly, the solidification behavior (e.g., solidification temperature range and amount/type of phases that form during solidification) provide an indication of resistance to solidification cracking. In this regard, alloys that show a relatively narrow solidification temperature range typically exhibit good resistance to solidification cracking. The hot ductility and solidification behavior of the experimental alloys are discussed in this section.

Hot ductility testing was conducted on alloys 0.4-A, 1-A, and 6, and the results are shown in Fig. 9. The reduction in area of each alloy reaches a maximum at ~950°C, and decreases significantly at temperatures below and above 950°C. In addition, the maximum ductility is a function of the Gd concentration, where increasing Gd reduces the peak reduction in area. The ductility is completely lost at temperatures above approximately 1060°C.

Figure 10 shows typical DTA scans acquired from alloys 1-A, 4, and 6. The heating scans are shown for alloys 1-A and 4, while both the heating and cooling scans are shown for alloy 6. The representative scans shown here are typical of those observed for the remaining alloys. For each alloy, there is a reaction that initiates at approximately 1060°C on heating. Note that the area under the peak, which is proportional to the energy released during the transformation and, therefore, the amount of phase that transforms during the reaction, increases with increasing Gd concentration. Considering that the volume fraction of $(\text{Fe,Ni,Cr})_3\text{Gd}$ increases with increasing Gd level (Ref. 10), it is reasonable to conclude that the reaction initiating at ~1060°C is liquation of the interdendritic Gd constituent. In addition, note that this liquation temperature is in excellent agreement with the hot ductility

curve shown in Fig. 9, where the ductility approaches zero near 1060°C. Liquation of a secondary phase is well known to induce significant reductions in ductility (Ref. 13). With continued heating, the liquation reaction is completed around 1090°C. There is often evidence of two separate liquation peaks in the DTA scans (e.g., for the 4 and 6 wt-% Gd alloys), suggesting there are two separate liquation events that occur on heating. The solidification behavior also exhibits two separate peaks on cooling — Fig. 10D. Figure 11 summarizes the DTA data, in which the average liquation and liquidus temperatures are plotted as a function of Gd concentration. The liquation temperature is essentially constant at ~1060°C, while the liquidus temperature decreases with increasing Gd concentration. It is important to note that the melting temperature range of these alloys in the as-cast condition varies from approximately 360° to 400°C. This range is extremely large and is responsible for the poor hot ductility displayed in Fig. 9.

A series of interrupted DTA scans was conducted in order to confirm that the low-temperature peaks were associated with liquation of the $(\text{Fe,Ni,Cr})_3\text{Gd}$ constituent. A 6 wt-% Gd sample was heated

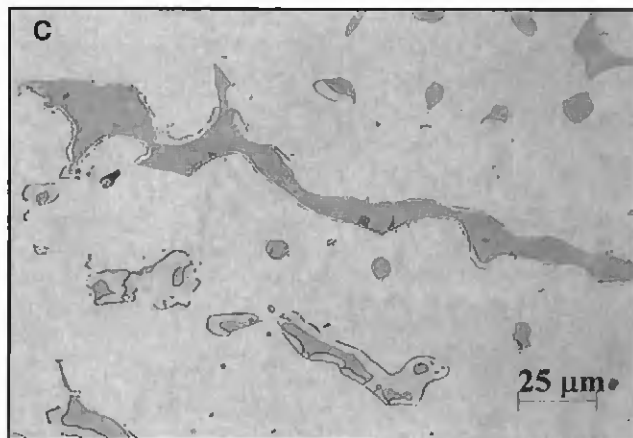
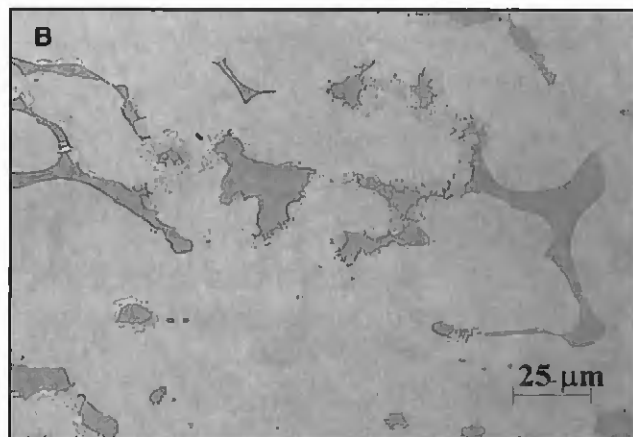
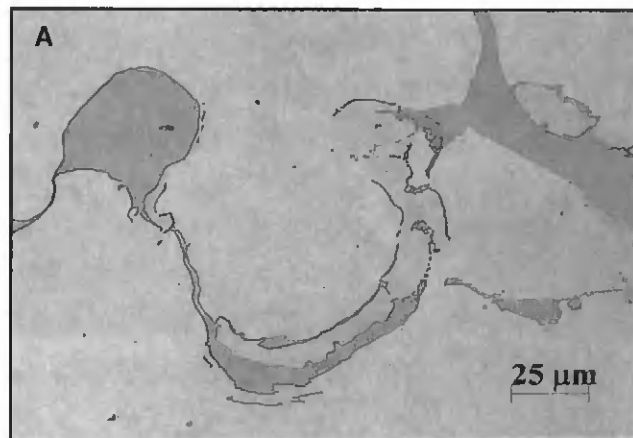


Fig. 12 — LOM photomicrographs showing DTA samples heated to the following: A — 1460°C; B — 1070°C; and C — 1135°C.

to a peak temperature of 1070°C, which is just above the liquation start temperature, and cooled. Similarly, a sample was heated to 1135°C, which is just above the liquation finish temperature, and cooled. These DTA samples were then metallographically compared to a sample that was heated to 1460°C where it was completely melted and then resolidified. Figure 12 shows the DTA samples from these three scans. The sample heated to 1460°C (Fig. 12A) shows a microstructure identical to the as-cast ingots, thus demonstrating that

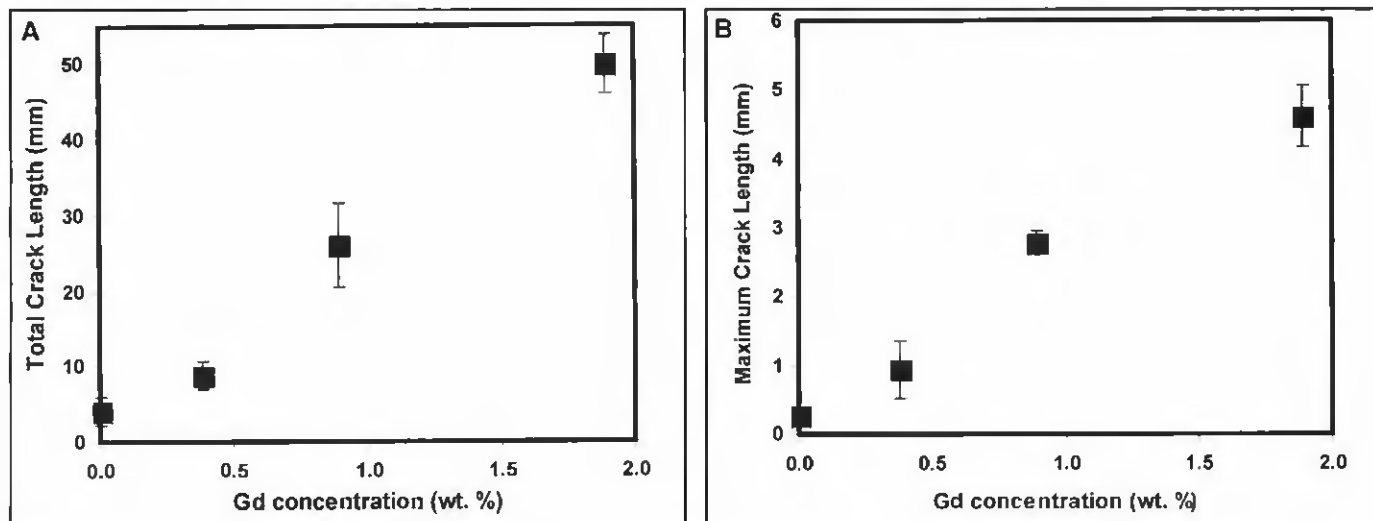


Fig. 13 — Varestraint weldability showing the following: A — Total crack length; and B — maximum crack length as a function of Gd concentration.

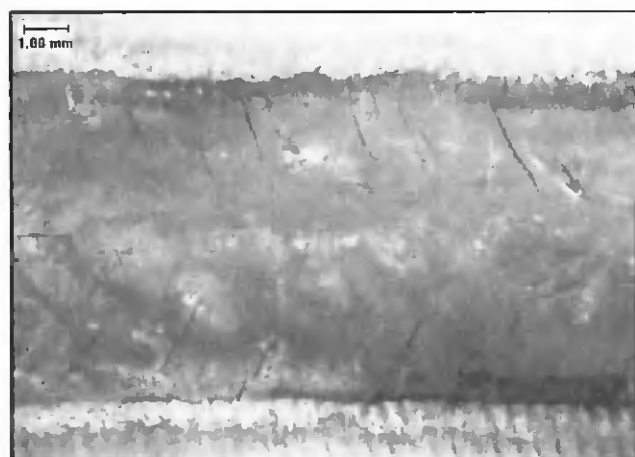


Fig. 14 — Cracking of Varestraint sample outside of the region where strain was applied.

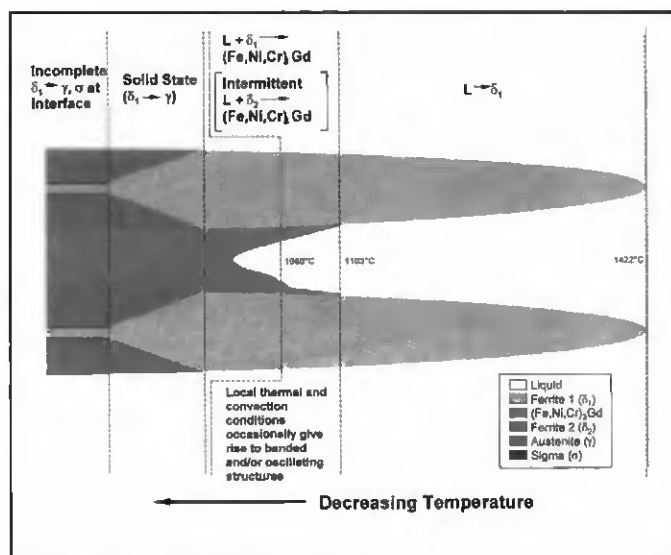


Fig. 15 — Proposed transformation sequence.

the temperatures derived from the DTA tests accurately reflect the reaction temperatures of the large-scale heats, and these are discussed further below in terms of the reaction sequences. The only exception here is formation of the sigma phase, which is not observed in the DTA samples. For the sample heated to 1070°C (Fig. 12B), there is direct evidence of liquation between the $(\text{Ni,Fe,Cr})_3\text{Gd}$ and the interdendritic ferrite. This suggests that liquation occurs in two separate steps, where the interdendritic ferrite first reacts with the surrounding $(\text{Ni,Fe,Cr})_3\text{Gd}$, followed by a second step where the remaining $(\text{Ni,Fe,Cr})_3\text{Gd}$ begins to react with the austenite. When the sample is heated above the liquation finish temperature, the original as-cast microstructure consisting of the full $(\text{Ni,Fe,Cr})_3\text{Gd}/\text{ferrite}/(\text{Ni,Fe,Cr})_3\text{Gd}$ morphology is re-

stored, demonstrating that the entire interdendritic constituent was completely molten at this temperature.

Weldability

Figure 13 shows the Varestraint data in terms of both the maximum and total crack lengths for the Gd-free 316L alloy in addition to alloys 0.4-B, 1-B, and 2. Microstructural examination of the as-cast ingot of the Gd-free alloy confirmed that it solidified by primary ferrite. Thus, this alloy is expected to exhibit good resistance to solidification cracking. The Varestraint results show that the solidification cracking susceptibility is very sensitive to the Gd concentration of the alloy, where extensive cracking is observed with increasing Gd concentration. In fact, as shown in Fig. 14, Varestraint samples exhibited severe

cracking outside of the test zone (i.e., in the region where no external strain was applied).

Discussion

Microstructural Evolution

The information presented in the previous sections can be used to understand the general microstructural evolution, hot ductility, and weldability of Gd-enriched stainless steels. The as-cast alloys exhibit four distinct phases: the austenite matrix, ferrite, $(\text{Ni,Fe,Cr})_3\text{Gd}$, and sigma. Ferrite is observed both in the cell cores and interdendritic regions. The DTA samples show peaks corresponding to these constituents, with the exception that sigma does not form under the DTA cooling conditions. There is essentially no Gd dis-

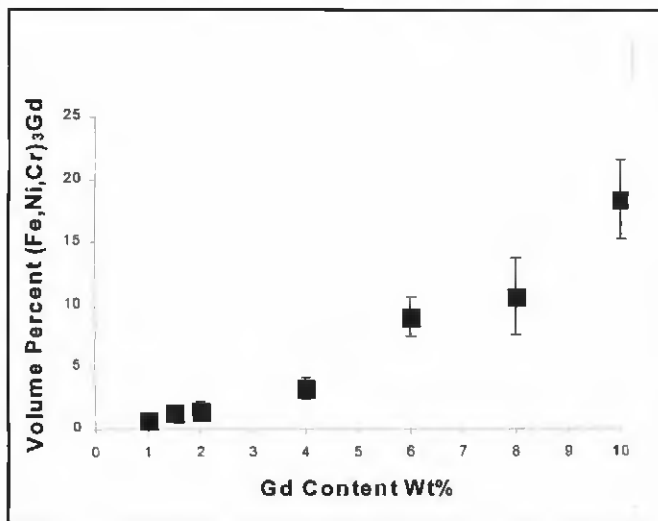


Fig. 16 — Variation in $(\text{Fe,Ni,Cr})_3\text{Gd}$ content with Gd concentration measured on small-scale, Gd-enriched stainless steels.

resolved in the austenite matrix or ferrite phases, and the $(\text{Ni,Fe,Cr})_3\text{Gd}$ phase is located in the interdendritic regions, indicating that it formed at the end of solidification. Ferrite, when present in the interdendritic regions, is generally surrounded by a thin layer of $(\text{Ni,Fe,Cr})_3\text{Gd}$.

For reference, the Welding Research Council (WRC) Ni_{eq} and Cr_{eq} values for each alloy are shown in Table 3 along with the expected solidification mode. Based on the 1992 WRC diagram (and initially disregarding the presence of the Gd), alloys 4 and 6 would be expected to solidify in the AF mode, while the remaining alloys would be expected to solidify in the FA mode. However, all the alloys contained ferrite in the cell/dendrite cores, which indicates that ferrite was the primary solidification phase for all the alloys. This suggests that the presence of Gd promotes primary ferrite solidification by shifting the δ/γ primary solidification phase boundary to higher Ni concentrations and lower Cr concentrations (i.e., the primary δ -ferrite phase field is enlarged with increasing Gd additions).

Additions of Gd can also affect the final ferrite content by formation of the $(\text{Ni,Fe,Cr})_3\text{Gd}$ phase that occurs near the end of solidification. As previously mentioned, recent research (Ref. 11) has shown that formation of the Ni-rich $(\text{Ni,Fe,Cr})_3\text{Gd}$ phase depletes the matrix of Ni and enriches the matrix in Cr and Mo. In fact, small-scale heats that were prepared in previous research (Ref. 11) with a nominal 316L composition and additions of 8 and 10 wt-% Gd exhibited a fully ferritic matrix due to extensive depletion of Ni and enrichment of Cr in the matrix, even though the nominal 316L composition had Ni and Cr concentrations

that were expected to produce a predominantly austenitic matrix. These observations demonstrate that selection of bulk composition aimed at forming an austenitic matrix must consider formation of the $(\text{Ni,Fe,Cr})_3\text{Gd}$ phase, and its concomitant effect on the matrix composition and phase stability. A quantitative mass balance technique for this purpose has recently been derived (Ref. 11) and was applied to the alloy compositions originally presented

in Table 1 to produce austenitic alloys that solidified in the FA mode. The fact that all the alloys exhibited a matrix that was predominately austenite with ferrite at the dendrite cores confirms that the technique is valid for these alloys.

The information presented above is used to propose a phase transformation sequence that accounts for the types and morphologies of phases observed experimentally. This transformation sequence is shown schematically in Fig. 15. Ferrite is observed in the cell cores, which indicates that solidification starts by the formation of primary ferrite. Primary ferrite solidification is known to be accompanied by rejection of Ni (and Gd) to the liquid and segregation of Cr and Mo to the ferrite (Ref. 13). Thus, the ferrite at the dendrite core is depleted in Ni and enriched in Cr and Mo relative to the ferrite in the interdendritic region. Since Gd is essentially insoluble in the ferrite (and austenite) phases, Gd segregates aggressively to the liquid during solidification. Primary ferrite solidification and Gd enrichment in the liquid continues until, at approximately 1100°C, the peritectic Liquid + Ferrite $\rightarrow (\text{Ni,Fe,Cr})_3\text{Gd}$ reaction initiates in the interdendritic regions. For much of the solidifying volume this reaction continues to completion — Figs. 3, 15. In other regions, however, a thin $(\text{Ni,Fe,Cr})_3\text{Gd}$ rim is also formed. This thin gadolinide constituent was shown to be connected to the major gadolinide, and to have the same composition, structure, and crystallographic orientation as the major gadolinide. It was also shown that when the thin rim is present, ferrite is always present between the rim and the major gadolinide. Finally, some interfaces on the rim were seen to display oscillating

features that were correlated spatially to similar features on the major gadolinide — Fig. 5.

The reasons for this interesting behavior are not readily apparent, but recent work by Tevedi and coworkers (Refs. 14–17) and summarized by Boettinger et al. (Ref. 18) provides at least a qualitative basis for understanding the microstructural development. Through experimental and modeling approaches, the referenced work has shown that a wide variety of microstructures (at least six variants have been classified) can develop in peritectic systems. In turn, these microstructures are strongly dependent on the convective and diffusion conditions prevalent during solidification. In particular, both handed (alternating primary and peritectic phases) and oscillatory structures (in which the primary and peritectic phases grow in oscillating continuous tree-like structures) appear to be present in the Gd-stainless steels. In this case, it is speculated that fluctuations in the local convection and thermal fields occasionally give rise to conditions favoring these microstructural variants. Following formation of a thin layer of peritectic gadolinide, in these locations new “secondary” ferrite is also formed (at approximately 1060°C). It is also surmised that this process also occasionally gives rise to the oscillatory structures. Just following solidification (i.e., before subsequent solid-state transformations), this sequence would produce a microstructure with the following spatial morphology: primary ferrite/ $(\text{Ni,Fe,Cr})_3\text{Gd}$ / “secondary” ferrite/ $(\text{Ni,Fe,Cr})_3\text{Gd}$, as observed experimentally in the rimmed regions. However, the primary ferrite is not stable during subsequent cooling and will transform to austenite by a diffusional transformation that involves rejection of Cr and Mo at the advancing austenite/ferrite boundary (Ref. 13). The transformation temperature of the ferrite \rightarrow austenite reaction is composition dependent, and regions of relatively high Ni and low Cr concentrations will transform at higher temperatures (Ref. 20). Since the interdendritic ferrite is higher in Ni and lower in Cr relative to that at the dendrite core, the ferrite \rightarrow austenite reaction is expected to initiate during cooling at the interdendritic region, with the austenite/ferrite boundary advancing back toward the dendrite core during subsequent cooling. The high Cr and Mo contents of the first ferrite that forms stabilize the ferrite at the dendrite core to lower temperatures, which accounts for the remnant primary ferrite observed at the dendrite cores.

The formation of austenite from the ferrite would lead to Cr and Mo rejection at the advancing interface, thus producing

Table 4 — Summary of Proposed Transformation Sequence

<u>Reaction</u>	<u>Comments</u>
<u>Solidification</u>	
1) Liquid → Ferrite	Liquid enriched in Ni and Gd
2) Liquid + Ferrite → (Ni,Fe,Cr) ₃ Gd	Liquid depleted in Ni and Gd
2a) In isolated regions. Liquid + "Secondary" Ferrite → (Ni,Fe,Cr) ₃ Gd	"Secondary" Ferrite depleted in Ni and enriched in Cr, Mo
<u>Solid-State Transformations</u>	
3) Primary Ferrite → Austenite	Causes Cr and Mo enrichment at primary ferrite/austenite boundary
4) Sigma nucleation and growth at ferrite/austenite boundary	Only observed in large-scale ingots (slower cooling rate)
5) Secondary Ferrite persists when surrounded by (Ni,Fe,Cr) ₃ Gd phase	(Ni,Fe,Cr) ₃ Gd phase acts as nucleation barrier to Ferrite → Austenite transformation

locally elevated Cr and Mo concentrations at the primary ferrite/austenite boundary. Sigma phase is known to nucleate at the austenite/ferrite boundaries where the local Cr and Mo content is high (Ref. 21), and this accounts for the presence of sigma observed at the austenite/ferrite boundaries in the large-scale heats. The lack of sigma at this location in the DTA samples is apparently related to cooling rate. Since sigma forms by a diffusional transformation, the cooling rate of the DTA samples after solidification was apparently too high for the solid-state reaction of sigma to occur. Lastly, comparison of Figs. 5 and 6 showed that ferrite persisted in the interdendritic regions only when the (Ni,Fe,Cr)₃Gd was present on both sides of the ferrite. According to the transformation sequence proposed here, this is the so-called "secondary" ferrite that forms after the first Liquid + Ferrite → (Ni,Fe,Cr)₃Gd peritectic-type reaction. As mentioned above, subsequent solid-state transformation of this ferrite to austenite requires redistribution of Cr and Mo. However, the Liquid + Ferrite → (Ni,Fe,Cr)₃Gd peritectic-type reactions can cause the secondary ferrite to be enveloped by the (Ni,Fe,Cr)₃Gd phase. Subsequent transformation of the secondary ferrite to austenite then requires diffusion of Cr, Mo, and Ni through the (Ni,Fe,Cr)₃Gd phase, but the diffusion rate of these substitutional elements is expected to be extremely slow through the intermetallic (Ni,Fe,Cr)₃Gd phase. Thus, the (Ni,Fe,Cr)₃Gd phase acts as a diffusion barrier and prevents subsequent solid-state transformation of the secondary ferrite. This explains why the secondary ferrite is stable to room temperature *only* when surrounded by the (Ni,Fe,Cr)₃Gd phase on each side — Fig. 5. When the (Ni,Fe,Cr)₃Gd phase is absent from one side, solid-state diffusion of

Cr and Mo can occur on this side (Fig. 6), thus permitting transformation of ferrite to austenite. The proposed transformation sequence is summarized in Table 4. The sequence proposed here accounts for the type and morphologies of phases observed experimentally and the dual peak observed in the DTA scans near 1060°C.

Solidification Cracking and Hot Ductility

The solidification cracking susceptibility is controlled primarily by the solidification temperature range and amount of terminal liquid that forms at the end of solidification. Alloys that exhibit a large solidification temperature range and form less than about 5–7 vol-% terminal liquid in a continuous or semicontinuous film along the grain boundaries and interdendritic regions are known to be most susceptible to cracking (Ref. 22). At larger volume fractions of terminal liquid, generally beyond 7–10 vol-%, backfilling of cracks by the terminal liquid can begin to occur, and cracking susceptibility is reduced with increasing amounts of terminal liquid.

The DTA results showed that these alloys exhibit a very wide solidification temperature range (360°–400°C). The amount of (Ni,Fe,Cr)₃Gd provides an indication of the amount of terminal liquid. Since there is essentially no Gd dissolved in the austenite or ferrite phases, all of the Gd is consumed in formation of the (Ni,Fe,Cr)₃Gd phase, and the amount of terminal Gd-rich liquid is expected to increase with increasing Gd concentration. This was observed experimentally. Figure 16 shows quantitative image analysis results in which the amount of (Ni,Fe,Cr)₃Gd phase was measured on small-scale Gd-enriched stainless steels with compositions similar to that used in this work (Ref. 11). As expected, these re-

sults show that the amount of (Ni,Fe,Cr)₃Gd increases with increasing Gd concentration. The results for alloys with less than 2 wt-% Gd are of interest to the weldability response. While alloys within this Gd concentration range show an increase in (Ni,Fe,Cr)₃Gd content with increasing Gd concentration, the volume fraction is always less than 5% when the Gd concentration is below 2 wt-%. Thus, no appreciable backfilling is expected in these alloys. The Varestreint test results show that hot cracking susceptibility increases substantially with increasing Gd concentration. Figure 11 shows that the solidification temperature range decreases moderately with increasing Gd concentration. Thus, the trend shown in Fig. 13 cannot be attributed to any factor related to the solidification temperature range because the solidification temperature range slightly decreases with increasing Gd concentration. Comparison of Figs. 13 and 16 shows that the maximum and total crack lengths increase with increasing (Ni,Fe,Cr)₃Gd content. Thus, based on these observations, the poor resistance to solidification cracking can generally be attributed to the very low Liquid + Ferrite → (Ni,Fe,Cr)₃Gd reaction temperature and concomitantly large solidification temperature range, while the increase in cracking susceptibility observed with increasing Gd concentration can be attributed to larger amounts of the low-temperature liquid that form as the Gd level is increased. As shown in Fig. 9, the hot workability is also significantly affected by the low-temperature (Ni,Fe,Cr)₃Gd phase since there is no substantial ductility above the liquefaction temperature of the (Ni,Fe,Cr)₃Gd phase.

Finally, it is interesting to note that, based on the Fe-Gd or Ni-Gd binary phase diagrams, formation of the (Ni,Fe,Cr)₃Gd phase is not expected for alloys with the Gd levels considered here. Based on these binary systems, (Fe,Ni)₁₇Gd₂ would be the first intermetallic expected to form during solidification for alloys within the Gd concentration range considered here. In the Ni-Gd system, the Ni₁₇Gd₂ phase forms by a terminal eutectic reaction for Gd levels below approximately 13 wt-% Gd. In the Fe-Gd system, the Fe₁₇Gd₂ forms first by a peritectic reaction that is followed by cascading peritectics involving the Fe₂₃Gd₆ and Fe₃Gd phases. Solidification then terminates with a eutectic reaction involving the Fe₂Gd phase. In any case, the equilibrium microstructure (based in the simple binary diagrams) is expected to be austenite and (Fe,Ni)₁₇Gd₂. The liquefaction temperature of the Fe₁₇Gd₂ and Ni₂₃Gd₆ phases is appreciably higher than that of the (Ni,Fe,Cr)₃Gd phase that is observed experimentally (1335°C in the Fe-

Gd system and 1275°C in the Ni-Gd system). This implies that heat treating of the as-cast material may promote dissolution of the low-temperature (Fe,Ni,Cr)₃Gd phase and formation of the higher-temperature (Fe,Ni)₁₇Gd₂ phase. However, a wide range of heat treatment temperatures (900° to 1270°C) and times (2 to 16 h) was recently investigated for this purpose, and it was found that the low-temperature (Fe,Ni,Cr)₃Gd phase cannot be dissolved under these heat treatment conditions. In fact, new higher gadolinides with even lower liquation temperatures were observed. Details of this study can be found in Ref. 10.

Conclusions

The physical and welding metallurgy of Gd-enriched stainless steels has been investigated with a combination of differential thermal analysis, Varesstraint and Gleeble tests, and various microstructural characterization techniques. The following conclusions can be drawn from this research.

1) Solidification of these alloys occurs in the primary ferrite mode and terminates by a peritectic reaction involving the (Fe,Ni,Cr)₃Gd phase. The ferrite partially transforms to austenite after solidification by a solid-state transformation, producing a final microstructure that has an austenitic matrix with remnant ferrite at the dendrite cores and interdendritic (Fe,Ni,Cr)₃Gd. Locally complex convective and thermal fields can occasionally give rise to complex variants in the peritectic microstructures.

2) The solidification temperature range of these alloys is very large (360° to 400°C, depending on Gd concentration) due to formation of the (Fe,Ni,Cr)₃Gd phase.

3) The hot ductility is lost above ~1060°C due to liquation of the (Fe,Ni,Cr)₃Gd phase, which severely limits the ability to form these alloys by high-temperature deformation techniques such as rolling and hot forging.

4) The alloys exhibit a high susceptibility to solidification cracking. The poor cracking resistance observed for all the Gd-containing alloys is attributed to the large solidification temperature range associated with the peritectic formation of the (Fe,Ni,Cr)₃Gd phase. The increase in cracking susceptibility observed with increasing Gd concentration is attributed to increased amounts of Gd-rich liquid that exist at the end of solidification.

Acknowledgments

This work was supported by the U.S. Department of Energy, Assistant Secretary for Environmental Management, under DOE Idaho Operations Office

Contract No. DE-AC07-99ID13727. This work was performed at Lehigh University, Sandia National Laboratories, and Idaho National Engineering and Environmental Laboratory through support from the National Spent Nuclear Fuel Program. Sandia is a multiprogram laboratory operated by Sandia Corp., a Lockheed Martin Company, for the U.S. Department of Energy under Contract DE-AC04-94AL8500.

References

- Hull, L., Pace, M., Lessing, P., Rogers, R., Mizia, R., Propp, A., Shaber, E., and Taylor, L. 2000. *Advanced Neutron Absorbers for DOE SNF Standardized Casks — Feasibility Study*. Idaho National Engineering and Environmental Laboratory Report DOE/SNF/REP-057 Rev. 0.
- Robino, C. V., and Cieslak, M. J. 1997. Fusion welding of a modern borated stainless steel. *Welding Journal* 76(1): 11-s to 23-s.
- Robino, C. V., and Cieslak, M. J. 1995. *Metallurgical and Materials Transactions A* 26A: 1673-1685.
- Van Konynenburg, R. A., Curtis, P. G., Summers, T. S. E. 1998. *Scoping Corrosion Tests on Candidate Waste Package Basket Materials for the Yucca Mountain Project*. Report UCRL-ID-130386, Lawrence Livermore National Laboratory.
- Zheng, J., and Zhou, H. 1986. The phase diagram of Fe-gadolinium-Ni ternary system. *Zhongguo Xitu Xuebao (Journal of the Chinese Rare Earth Society)* 4(2): 79-81.
- Metals Handbook*, Vol. 3. 1992. Binary alloy phase diagrams. Materials Park, Ohio: ASM International.
- Zinkevitch, M., Mattern, N., Wendrock, H., Behr, G., and Wetzig, K. 1999. Solidification behavior of Fe-gadolinium-Mo alloys. *Journal of Alloys and Compounds* 283: 265-281.
- Personal communication with G. J. Del Corso, Carpenter Technology Corporation, Reading, Pa., September 1999.
- DuPont, J. N., Robino, C. V., Mizia, R. E., Michael, J. R., and Williams, D. B. Physical and welding metallurgy of Gd-enriched austenitic alloys for spent nuclear fuel applications, Part II: Nickel-base alloys. To be published in the *Welding Journal*.
- DuPont, J. N., Liu, Z. Q., Banovic, S. W., Williams, D. B., Robino, C. V., Stephens, J. J., McConnell, P. M., Mizia, R. E., Shaber, E. L., Branagan, D. J. 2001. *Development of Gadolinium-Containing Stainless Steels*. Idaho National Engineering and Environmental Laboratory Report, DOE/SNF/REP-066.
- Robino, C. V., DuPont, J. N., Mizia, R. E., Michael, J. R., Williams, D. B., and Shaber, E. 2003. Development of Gd enriched alloys for spent nuclear fuel applications — Part I: Preliminary characterization of small scale Gd enriched stainless steels. *Journal of Materials Engineering and Performance* Vol. 12, No. 2, April, pp. 206-214.

12. Goldstein, J. I., et al. 1992. *Scanning Electron Microscopy and X-ray Microanalysis* 2nd ed. New York, N.Y.: Plenum Press.

13. Brooks, J. A., and Thompson, A. W. 1991. *International Materials Reviews*, 36(1): 16-44.

14. Tevedi, R. 1995. Theory of layered-structure formation in peritectic systems. *Metallurgical and Materials Transactions A*, 26A: 1583-1590.

15. Park, J. S., and Tevedi, R. 1998. Convection-induced novel oscillating microstructure formation in peritectic systems. *Journal of Crystal Growth* 187: 511-515.

16. Mazumder, P., Tevedi, R., and Karma, A. 2000. A model of convection-induced oscillatory structure formation in peritectic alloys. *Metallurgical and Materials Transactions A* 31A: 1233-1246.

17. Tevedi, R., Miyahara, H., Mazumder, P., Simsek, E., and Tewari, S. N. 2001. Directional solidification microstructures in diffusive and convective regimes. *Journal of Crystal Growth* 222: 365-379.

18. Boettinger, W. J., Coriell, S. R., Greer, A. L., Karma, A., Kurz, W., Rappaz, M., and Tevedi, R. 2000. Solidification microstructures: Recent developments, future directions. *Acta Materialia*, 48: 43-79.

19. Knorovsky, G. A., Cieslak, M. J., Headley, T. J., Romig, A. D., and Hammett, W. F. 1989. *Metallurgical Transactions A* 20A: 2149-2158.

20. Rivlin, V. G., and Raynor, G. V. 1980. Critical evaluation of constitution of Cr-Fe-Ni system. *International Materials Reviews* 1: 21-38.

21. Gunn, R. N. 1997. *Duplex Stainless Steels*. Cambridge, England: Abington Publishing.

22. Clyne, T. W., and Kurz, W. 1982. The effect of melt composition on solidification cracking of steel, with particular reference to continuous casting. *Metall. Trans. B* 13A: 259-266.

Do You Have Some News to Tell Us?

If you have a news item that might interest the readers of the *Welding Journal*, send it to the following address:

Welding Journal Dept.
Attn: Mary Ruth Johnsen
550 NW LeJeune Rd.
Miami, FL 33126.

Items can also be sent via FAX to (305) 443-7404 or by e-mail to mjohnsen@aws.org.